Journal of Electron Spectroscopy and Related Phenomena 266 (2023) 147355

Contents lists available at ScienceDirect

Journal of Electron Spectroscopy and Related Phenomena

journal homepage: www.elsevier.com/locate/elspec

Illuminating the brain: Revealing brain biochemistry with synchrotron X-ray spectromicroscopy

James Everett [a,b,*], Jake Brooks [b], Frederik Lermyte [b,c], Vindy Tjendana Tjhin [b], Ian Hands-Portman [d], Emily Hill [d], Joanna F. Collingwood [b], Neil D. Telling [a,**]

[a] School of Pharmacy and Bioengineering, Guy Hilton Research Centre, Thornburrow Drive, Keele University, Staffordshire ST4 7QB, UK
[b] School of Engineering, University of Warwick, Library Road, Coventry CV4 7AL, UK
[c] Department of Chemistry, Technical University of Darmstadt, Alarich-Weiss-Strasse 4, 64287 Darmstadt, Germany
[d] School of Life Sciences, Gibbet Hill Campus, University of Warwick, Coventry CV4 7AL, UK

ARTICLE INFO

Keywords:
Scanning transmission X-ray microscopy
Neurodegenerative Disease
Neuromelanin
Corpora amylacea
Correlative microscopy
Brain metals

ABSTRACT

The synchrotron x-ray spectromicroscopy technique Scanning Transmission X-ray Microscopy (STXM) offers a powerful means to examine the underlying biochemistry of biological systems, owing to its combined chemical sensitivity and nanoscale spatial resolution. Here we introduce and demonstrate methodology for the use of STXM to examine the biochemistry of the human brain. We then discuss how this approach can help us better understand the biochemical changes that occur during the development of degenerative brain disorders, potentially facilitating the development of new therapies for disease diagnosis and treatment.

1. Introduction

Elucidating the biochemistry of biological systems is key to understanding their roles, both in normal physiology and pathology. The human brain is a highly complex organ that is reliant on a wide array of essential chemical elements and compounds to maintain normal function. This complexity is reflected in the brain's vast structural and chemical heterogeneity, with differing brain regions exhibiting distinct cell populations, functionality, and chemical composition [1]. Thus, to define the biochemistry of the brain, techniques combining excellent chemical sensitivity with high resolution imaging capabilities are essential. Discovering this information is critically important; not only in understanding the physiological functions of the brain, but also to probe the biochemical changes that occur during ageing and pathological processes, such as those involved in the onset and progression of degenerative brain disorders including Alzheimer's and Parkinson's disease. Better understanding how the biochemical environment is altered in the diseased brain strongly supports the development of viable physico-chemical technologies for disease diagnosis and treatment.

One technique that offers chemically-sensitive nanoscale resolution imaging is x-ray spectromicroscopy in the form of STXM. This synchrotron-based approach is equipped for elemental composition analysis, as well as speciation analysis to distinguish specific compounds or chemical states of a given element (e.g. differing transition metal oxidation states). Consequently, STXM has greater chemical sensitivity compared to x-ray elemental mapping alone. The typical large operational energy range of scanning transmission x-ray microscopes allows access to signals from both organic and inorganic compounds. When considering the biochemical composition of brain tissues, this unique combined chemical and spatial sensitivity enables a chemical fingerprint to be determined for highly localized regions of interest, such that anatomical features can be mapped in isolation, crucially without requirement for chemically disruptive staining or contrast agents. This includes specific cell types, subcellular components, and even pathological features.

Here we introduce methodology for the STXM examination of human brain tissues, and discuss the recent applications of these techniques by our group to investigate the role of metals in neurodegenerative disorders. We describe the process of using spectromicroscopy to identify x-ray absorption features associated with specific brain structures, and how this information can be used to map the chemical profile of brain tissue sections. In this article we explore a small number of example datasets, taken from our broader work to understand the biochemistry of the brain, to demonstrate the measurement capabilities of STXM, that

* Corresponding author at: School of Pharmacy and Bioengineering, Guy Hilton Research Centre, Thornburrow Drive, Keele University, Staffordshire ST4 7QB, UK.
** Corresponding author.
E-mail addresses: j.everett@keele.ac.uk (J. Everett), n.d.telling@keele.ac.uk (N.D. Telling).

https://doi.org/10.1016/j.elspec.2023.147355
Received 28 February 2023; Received in revised form 12 June 2023; Accepted 12 June 2023
Available online 16 June 2023

are.

2. Materials and methods

Human brain tissue was obtained at autopsy with informed consent. Brain tissue samples were prepared and analysed under UK ethical approvals 07/MRE08/12 and REGO-2018–2223.

3. Embedding of brain tissue

Brain tissue was embedded and sectioned for STXM analysis as previously described in [2]. Tissues were embedded in an equimolar mixture of trimethylolpropane triglycidyl ether: 4,4′-methylenebis (2 methylcyclohexylamine) extensively used by our group for the examination of biological tissues using synchrotron x-ray spectromicroscopy [2–6]. Semi-thin sections of embedded tissues were cut to either 500 or 200 nm thickness using a Reichert-Jung Ultra-cut microtome operating with a non-metallic (diamond) blade. Tissue sections were deposited onto copper TEM grids (Agar Scientific; 100 mesh) and these grids were then mounted onto STXM sample plates for x-ray spectromicroscopy analysis.

4. Scanning transmission x-ray microscopy

X-ray spectromicroscopy experiments were performed using STXM at the Advanced Light Source beamline 11.0.2 (Lawrence Berkeley National Laboratory, CA, USA), Diamond Light Source beamline I08 (Oxfordshire, United Kingdom), Canadian Light Source SM beamline (Saskatoon, Canada) and MAX IV SoftiMAX beamline (Lund, Sweden). Focused x-ray spot sizes were $\leq$ 50 nm. X-ray photon doses were kept as low as possible while maintaining sufficient signal-to-noise ratios, thus minimizing photon-dose effects and substantial alterations to native sample (bio)chemistry. This was achieved by controlling dwell (exposure) times per pixel as well as using small beamline exit slit sizes. For further information on our evaluation of optimized STXM parameters for the examination of brain tissues, see the Supplementary Materials of [5]. Raw x-ray absorption intensities were normalized to the incident x-ray beam by conversion to optical density using appropriate background regions see for e.g., [2,5,6].

To map the distribution of chemical species within brain tissues, paired images were taken: one at the energy corresponding to the absorption feature of interest and a second at an off-peak energy a few eV away from the feature. Following conversion to optical density, the off-peak image was then subtracted from the peak image to create a difference (speciation) map. Additional iron oxidation state difference maps were created by subtracting images taken at absorption energies corresponding to low oxidation state iron forms such as Fe^{2+}/Fe^{0} (708 eV) iron, from oxidized Fe^{3+} (709.5 eV). These maps provide a qualitative distribution of the different iron oxidation states present within the region.

X-ray absorption spectra providing detailed information regarding the chemical state of the samples were obtained from a series of images (called a "stack") taken over a desired energy absorption edge. X-ray absorption spectra were collected over the carbon and oxygen *K*-edges and the iron L_3-edge. For carbon *K*-edge measurements, x-ray absorption spectra were corrected for the embedding resin by subtracting the resin component from the tissue spectrum as described in [6] and [2].

Where multiple images were taken at different energies (i.e. speciation maps/stacks), images were aligned to a common feature, compensating for any movement in the sample or x-ray beam position that may have occurred during scanning.

STXM data were processed using the aXis 2000 software package (http://unicorn.mcmaster.ca/aXis2000.html). Cross-correlation analysis was used to align the images. Greyscale x-ray microscopy images were converted to false colour and recombined as overlays to create pseudo-coloured composite images using the ImageJ software. To remove interference patterns caused by the injection of electrons into the synchrotron storage ring (so-called "top-up"), a bandpass image filter was applied using ImageJ (applicable to Fig. 7 only).

5. Histology

5.1. RNA staining

Immunostaining for RNA was used to reveal the distribution of cellular material in tissue sections using RNASelect green fluorescent cell stain (ThermoFisher; S32703). Antigen retrieval was performed via heat-induced epitope retrieval using a buffer of 10 mM sodium citrate and 0.05% Tween 20, adjusted to pH 6.0 with HCl and heated to 90 degrees. Prior to immunostaining, a blocking solution of (1% BSA, 0.4% Triton 100X in PBS) was applied for 20 min. Immunostaining was performed using primary antibody SYTO RNASelect green fluorescent cell stain, diluted 1:10000 and applied to tissue sections for 1 h.

Immunofluorescent imaging was performed using a Zeiss LSM 880 confocal microscope, equipped with three photomultiplier detectors and a Gallium Arsenide Phosphide (GASP) detector. Fluorescence was stimulated by scanning with a laser of wavelength 490 nm. Images were acquired in fluorescence and bright field modes.

5.2. Toluidine blue staining

Toluidine blue was used as a histological stain to image tissue ultrastructure in tissue sections. 20 mg of sodium tetraborate decahydrate was dissolved in deionized ultrapure water (dH_2O). 10 mg of toluidine blue powder was added until dissolved, then the solution was filtered. 2 uL of staining solution was pipetted onto tissue sections whilst the glass slide substrate was heated using a hot plate operating at 70 °C. Excess staining solution was rinsed off with dH_2O after 1 min, before light microscope imaging.

6. Results

6.1. Imaging tissue ultrastructure

When determining the nanoscale chemical composition of organs such as the brain, the visualization of tissue ultrastructure is a critical step necessary to provide biological context, owing to the complex and spatially heterogeneous biochemistry of these sample types.

To visualize the ultrastructure of brain tissue sections using STXM in the soft x-ray regime, spectromicroscopy performed at the carbon *K*-edge and oxygen *K*-edge is highly effective, albeit dependent on sample thickness. For tissue sections ca. $<$ 200 nm in thickness, the carbon *K*-edge (280–320 eV) is preferentially used. Tissue sections thicker than 200 nm are prone to saturation of incident x-ray beam at the carbon *K*-edge. The higher energy oxygen *K*-edge (530–545 eV) is therefore used to permit ultrastructure visualisation in sections of 200–500 nm thickness.

Fig. 1 shows carbon *K*-edge STXM data from hippocampus and amygdala tissue sections from two Alzheimer's disease cases, and the substantia nigra of a Parkinson's disease case. Fig. 1A shows a representative carbon *K*-edge x-ray absorption spectrum collected from brain tissue parenchyma by performing spectromicroscopy over the carbon *K*-edge. The spectrum is dominated by a white line peak at ca. 288.3 eV corresponding to the to the C 1 s→π * transition for the C═O bond of the amide group (i.e. carboxamide group) found in peptide bonds [7,8]. This absorption feature provides an ideal means to visualize tissue ultrastructure due to the high amide bond content of brain tissue and the absence of amide groups in the embedding resin. In addition, the high intensity ("jump") of the π * absorption feature provides excellent absorption contrast against background (non-specific) absorption artefacts, allowing for well-defined, high resolution tissue speciation maps to be created. Although collected from the Alzheimer's disease

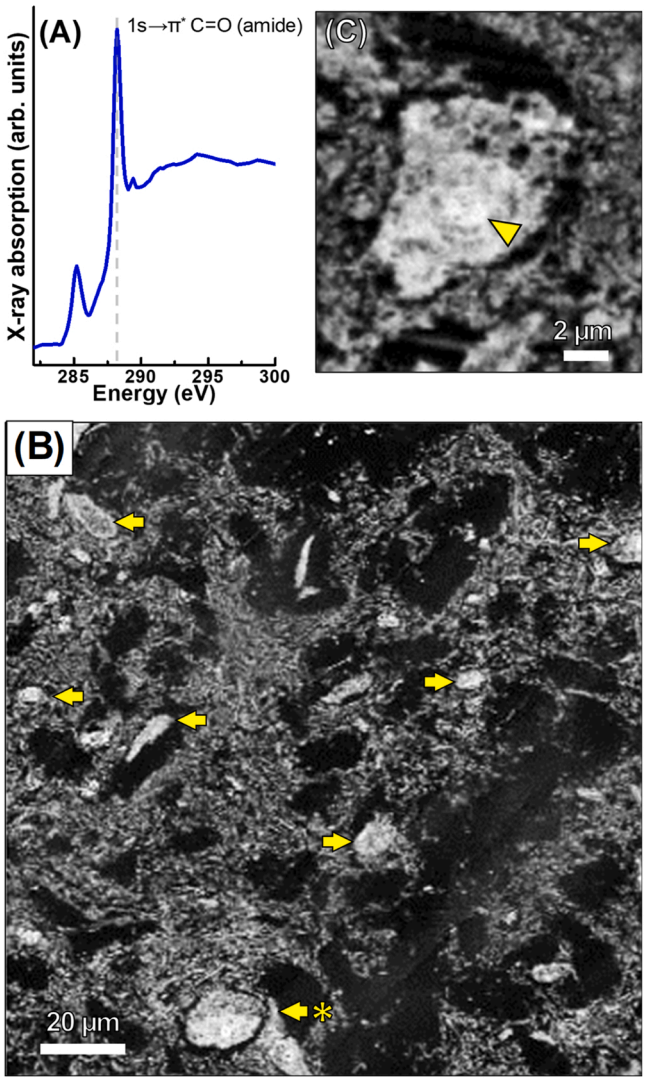

Fig. 1. Carbon *K*-edge STXM examination of 200 nm thick brain tissue sections. **(A)** A typical x-ray absorption spectrum from brain tissue parenchyma. The principal 288.3 eV (amide) absorption feature is highlighted by the dotted line. Data collected from a hippocampal tissue section. (B-C) Tissue speciation maps collected at 288.3 eV showing tissue ultrastructure. **(B)** 450 nm resolution map of a substantia nigra tissue section where multiple cells (examples highlighted by arrows) are apparent against the extracellular neuropil. A dopaminergic neuron is highlighted by the asterisk. **(C)** 200 nm resolution map of a cell within an amygdala section. The cell nuclelus/nucleolus is highlighted by the arrowhead.
Data acquired at MAX IV SoftiMAX beamline and Advanced Light Source beamline 11.0.2.

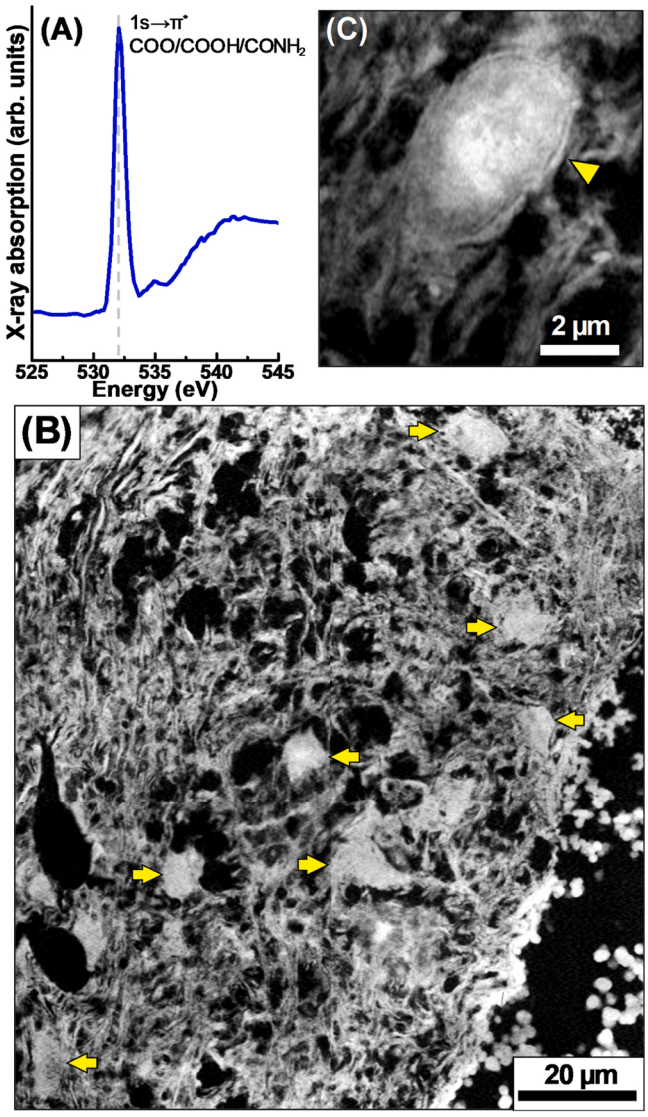

Fig. 2. Oxygen *K*-edge STXM examination of a 500 nm thick brain section of Alzheimer's disease putamen. **(A)** A typical x-ray absorption spectrum from the brain tissue parenchyma. The principal 532.1 eV absorption feature is highlighted by the dotted line. (B-C) Tissue speciation maps collected at 532.1 eV showing tissue ultrastructure. **(B)** 100 nm resolution map of a tissue region where multiple cells (highlighted by arrows) can be seen against the extracellular neuropil. In the lower right quadrant of the image a blood vessel can be observed containing probable red blood cells. **(C)** 100 nm resolution map of a cell. The cell membrane is highlighted by the arrowhead.
Data acquired at Advanced Light Source beamline 11.0.2.

hippocampus in this instance, in practice we have demonstrated this absorption feature to be consistent across different brain regions and disease states.

Examples of carbon *K*-edge tissue speciation maps from 200 nm thick sections of brain tissue are displayed in Fig. 1B-C. Fig. 1B is a large tissue speciation map taken at 450 nm resolution, where multiple cells of differing morphologies can be observed distributed throughout the neuropil. Using such maps, it is possible to positively identify specific cell types, such as the dopaminergic neuron highlighted by the asterisk. Fig. 1C shows a cell imaged to 200 nm spatial resolution. In this tissue map intracellular organelles (nucleus and nucleolus) can be discerned (arrowhead).

Fig. 2 shows oxygen *K*-edge datasets collected from 500 nm thick putamen tissue sections from an Alzheimer's disease case. A typical oxygen *K*-edge spectrum from the brain tissue parenchyma is shown in Fig. 2A. This spectrum is dominated by a single white line peak at 532.1 eV, corresponding to the O 1 s→π* transition for COO/COOH/$CONH_2$ groups [9]. This feature can be used to create oxygen *K*-edge tissue speciation maps, as shown in Fig. 2B-C. Fig. 2B shows a large 100 nm resolution tissue map, where cells can be observed against the extracellular neuropil. This large map represents a compound image composed of multiple smaller images. Fig. 2C shows a cell imaged to 100 nm spatial resolution displaying a recognizable cell membrane.

Once the prevailing tissue ultrastructure is determined, the distribution and chemical state of further classes of organic and bioinorganic compounds can be placed into biological context. In the following three sections we provide examples of how STXM can be used to discriminate specific biological structures and chemical compounds against the surrounding tissue ultrastructure.

7. Neuromelanin mapping in the substantia nigra region of the brain

Neuromelanin (NM) is a biological polymer formed in the central nervous system by the autoxidation of dopamine and cysteine. It is most concentrated in dopaminergic neurons of the substantia nigra pars compacta and locus coeruleus [2,10]. This pigment, structurally related to melanin, is contained within organelles 0.5–3 μm in size containing NM clusters 200–600 nm in size, which are divided into spherical granules of ca. 30 nm diameter. NM has been proposed as the main chelator of neuronal iron in the substantia nigra, suggesting a role in neuroprotection under physiological conditions. [10].

Fig. 3 shows carbon *K*-edge STXM analysis of dopaminergic neurons within a 200 nm thick substantia nigra section. Displayed in Fig. 3A is an (amide) tissue map revealing cellular ultrastructure against the surrounding neuropil. Spectromicroscopy performed on this tissue area over the entire carbon *K*-edge shows spatial variation in carbon chemistry *within* the neurons (Fig. 3D). The carbon *K*-edge x-ray absorption spectrum from area D1 (blue spectrum) is consistent with the archetypal tissue spectrum shown in Fig. 1A. Conversely, the spectrum from area D2 (red spectrum) contains an additional absorption feature ca. 1.1 eV below the amide peak that is absent in spectrum D1 and Fig. 1A. This 287.2 eV feature corresponds to the 1 s–σ * (C−S) transition derived from the benzothiazine groups of NM (Fig. 3E red) [2], and can be used to visualize NM within the prevailing tissue ultrastructure, as demonstrated in Fig. 3B-C. Note due to slight differences in energy calibration between experiments/ STXM beamlines, the energy position of the NM peak corresponds to that previously reported by our group in [2] by subtracting 0.2 eV. As the sulphur *K* and *L*-edges fall within the usable energy range of select STXM beamlines, it should also be feasible to visualise NM at these edges by exploiting the sulphur content of benzothiazine. Indeed, we have previously used sulphur elemental mapping using synchrotron x-ray fluorescence (XRF) to visualize NM content (Figure S6, [2].

8. Revealing the chemical signature of corpora amylacea microstructures in the brain

A commonly occurring microstructure that forms in the human brain are corpora amylacea (CA), polyglucosan bodies which increase in number and size with age. While primarily composed of polymerised hexoses containing both α-1:4 and α-1:6 glucosidic linkages, numerous

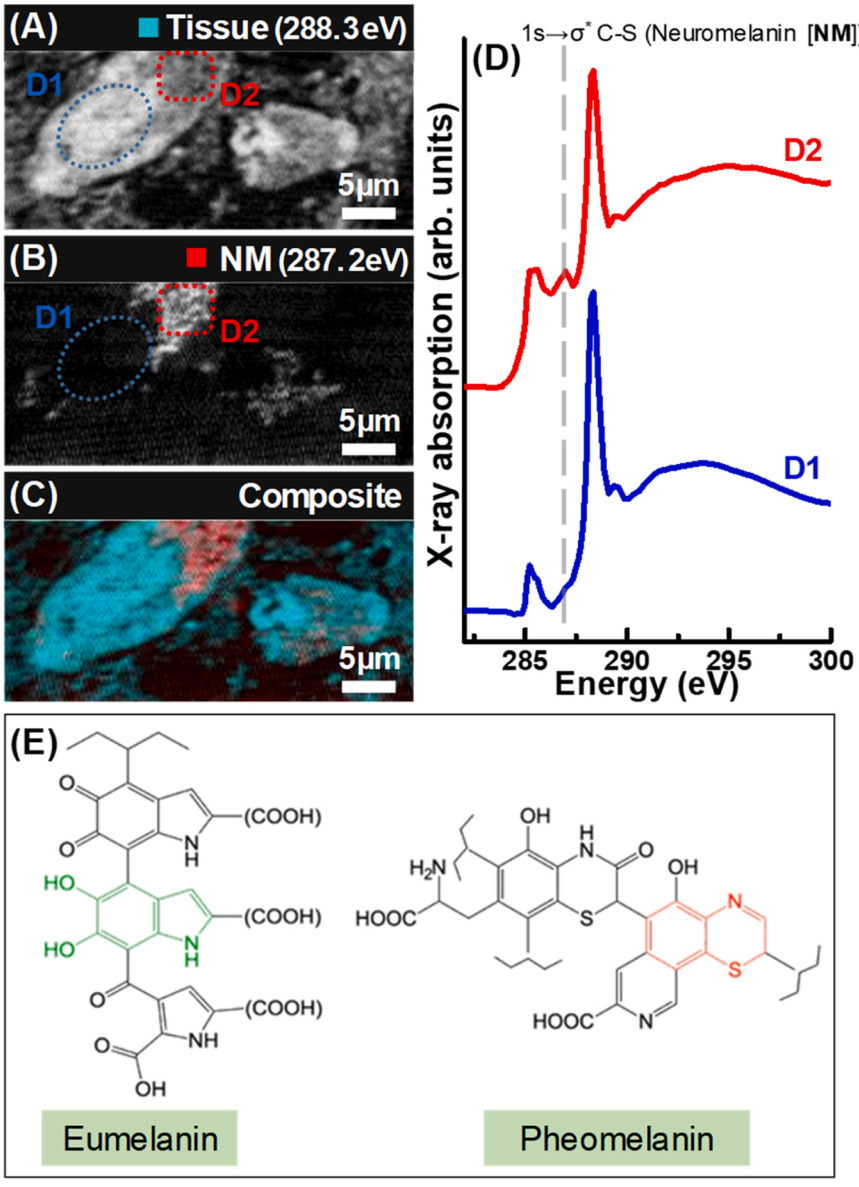

Fig. 3. Carbon *K*-edge STXM analysis of neuromelanin (NM) containing dopaminergic neurons within a 200 nm thick substantia nigra tissue section. **(A)** Tissue speciation map showing the overall ultrastructure. **(B)** NM speciation map collected using the NM specific absorption feature at 287.2 eV identified in (D). **(C)** Composite image showing tissue ultrastructure in cyan and NM distribution in red. **(D)** Carbon *K*-edge x-ray absorption spectra from the cellular areas highlighted in panels (A) and (B). The 287.2 eV NM absorption feature is highlighted by the dotted grey line. **(E)** Structures of eumelanin (NM surface) and pheomelanin (NM core). The benzothiazine group of pheomelanin is labelled in red.
(a) Modified from Brooks et al. [2,11]. (b) Data acquired at Diamond Light Source beamline I08.

further components postulated to be derived from neurons, oligodendrocytes, astrocytes and blood have been associated to CA. As a result of this diversity in constituents, their function is still not fully understood, but it has been suggested that they are involved in the clearance of biological waste products [12].

Fig. 4 shows carbon *K*-edge STXM analysis of two CA bodies (highlighted by asterisks) within a 200 nm thick section of brain tissue from the amygdala region. Fig. 4A shows a carbon *K*-edge x-ray absorption spectrum from CA (red trace) compared to the spectrum from the tissue parenchyma (blue trace). By comparing these spectra, it can be seen that CA contains a peak feature at 286.7 eV, that is absent in the parenchyma spectrum. The 286.7 eV speciation map displayed in Fig. 4C shows this feature can be used for the label-free imaging of CA against the surrounding tissue, further demonstrating how specific bond structures can be used to distinguish different brain tissue components. It is hoped this preliminary finding will allow the chemical composition of CA to be examined in greater detail, shedding light on the physiological function of these structures and their potential involvement in the development of polyglucosan disorders [13].

9. Mapping brain biominerals

A wide variety of biominerals incorporating numerous elements detectable using STXM are present in the human brain, and are integral components in processes required for healthy brain function. Here we will discuss three biomineral types frequently examined during our investigations into brain biochemistry: carbonates, calcium, and iron.

9.1. Carbonates

Carbonates (i.e. minerals containing CO_3^{2-}) are extremely varied, and are often found in compounds with metals such as calcium, magnesium and iron [14]. Using STXM, carbonates can be visualized by exploiting transitions at either the carbon *K*-edge or oxygen *K*-edge, as demonstrated in our previous examination of tissues derived from the human brain [3,4]. Fig. 5 shows STXM examination of two cells in close proximity within an Alzheimer's disease amygdala brain tissue section. Oxygen *K*-edge carbonate speciation mapping of the cells is shown in Fig. 5B, where a high level of carbonate accumulation can be seen intracellularly.

9.2. Calcium

Calcium is an integral co-factor in a multitude of neuronal functions including neurotransmitter synthesis and release, cell growth, neuronal excitability, synaptic transmission and plasticity [15]. STXM examination of calcium content within brain tissue sections can readily be assessed by exploiting calcium L_3 and L_2-edge absorption features (ca.

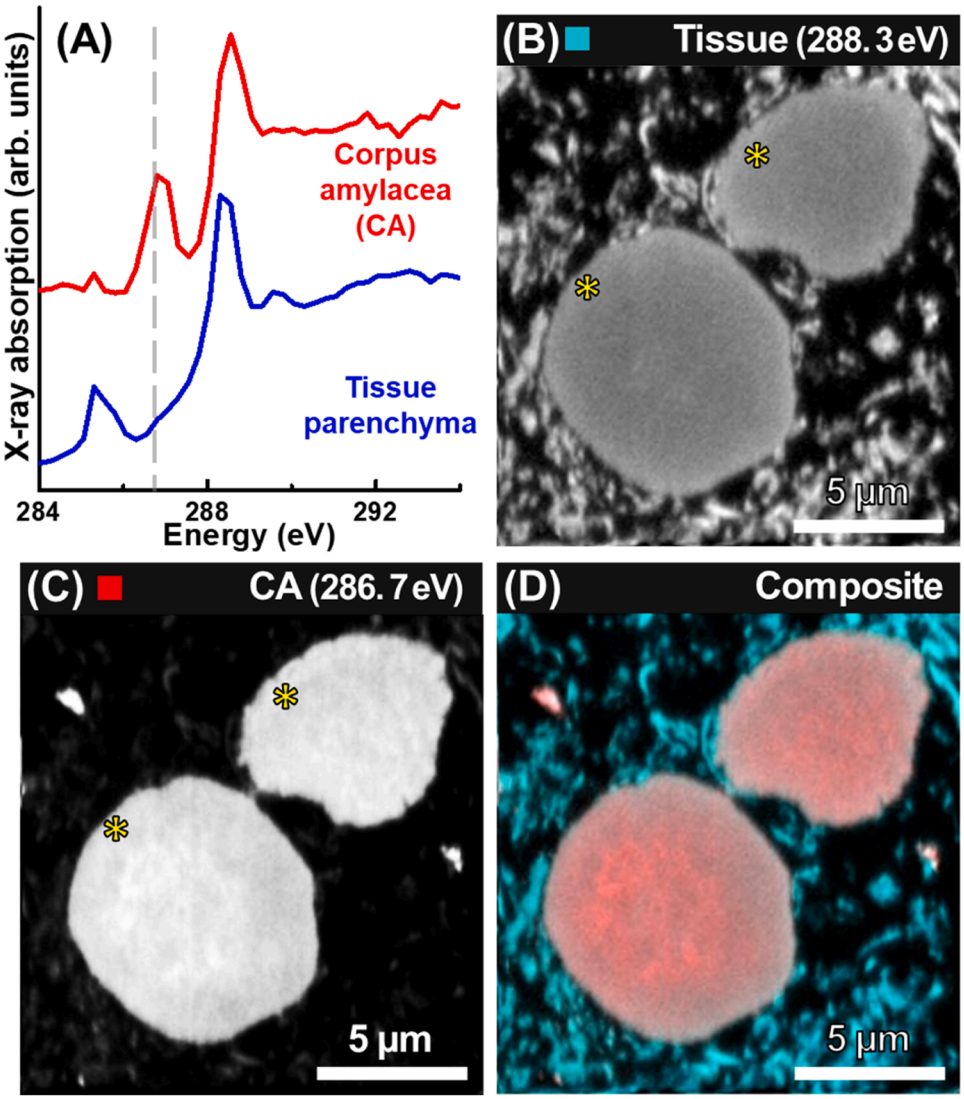

Fig. 4. Carbon *K*-edge STXM analysis of corpora amylacea within a 200 nm thick amygdala tissue section. **(A)** Carbon *K*-edge x-ray absorption spectra from corpora amylacea [red trace] and tissue parenchyma [blue trace]. The 286.7 eV absorption feature is highlighted by the dotted line. **(B)** Amide tissue map. **(C)** 286.7 eV map showing the corpora amylacea, which are also highlighted with asterisks in (B) and (C). Additional smaller fragments can be seen adjacent to the primary aggregates. **(D)** Composite image showing corpora amylacea in red, and the background neuropil in cyan.
Data acquired at Diamond Light Source beamline I08.

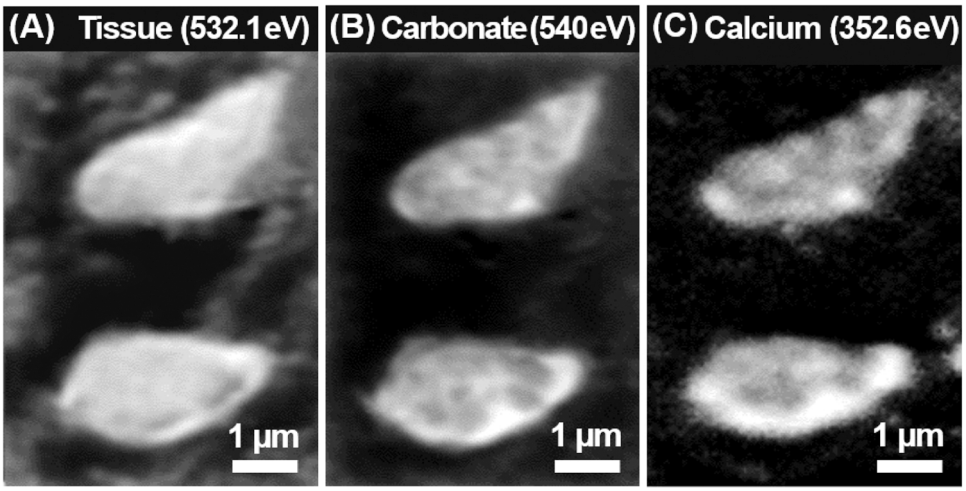

Fig. 5. STXM analysis of cellular material from a 500 nm thick section of Alzheimer's disease amygdala. **(A)** Oxygen *K*-edge tissue map. **(B)** Oxygen *K*-edge carbonate map. **(C)** Calcium *L*-edge map.
Data acquired at Diamond Light Source beamline I08.

349.3 and 352.6 eV respectively) [16,17]. This is demonstrated in Fig. 5C, where calcium can be seen to be accumulated within the cellular bodies. This pattern of accumulation is consistent with the carbonate map shown in Fig. 5B suggesting the presence of calcium carbonate within the cells.

Disrupted calcium homeostasis, and hyper-biomineralization of tissues is associated with human diseases including neurodegenerative disorders, while levels of intracellular Ca^{2+} are increased in aged neurons [3,4,18]. As the cells shown in Fig. 5 are from an elderly patient afflicted with Alzheimer's, the observed high levels of intracellular calcium and carbonate may be a consequence of disrupted calcium homeostasis, occurring as a result of the ageing process.

While the examples shown in Fig. 5 demonstrate a means of visualizing the prevailing calcium and carbonate distribution within biological

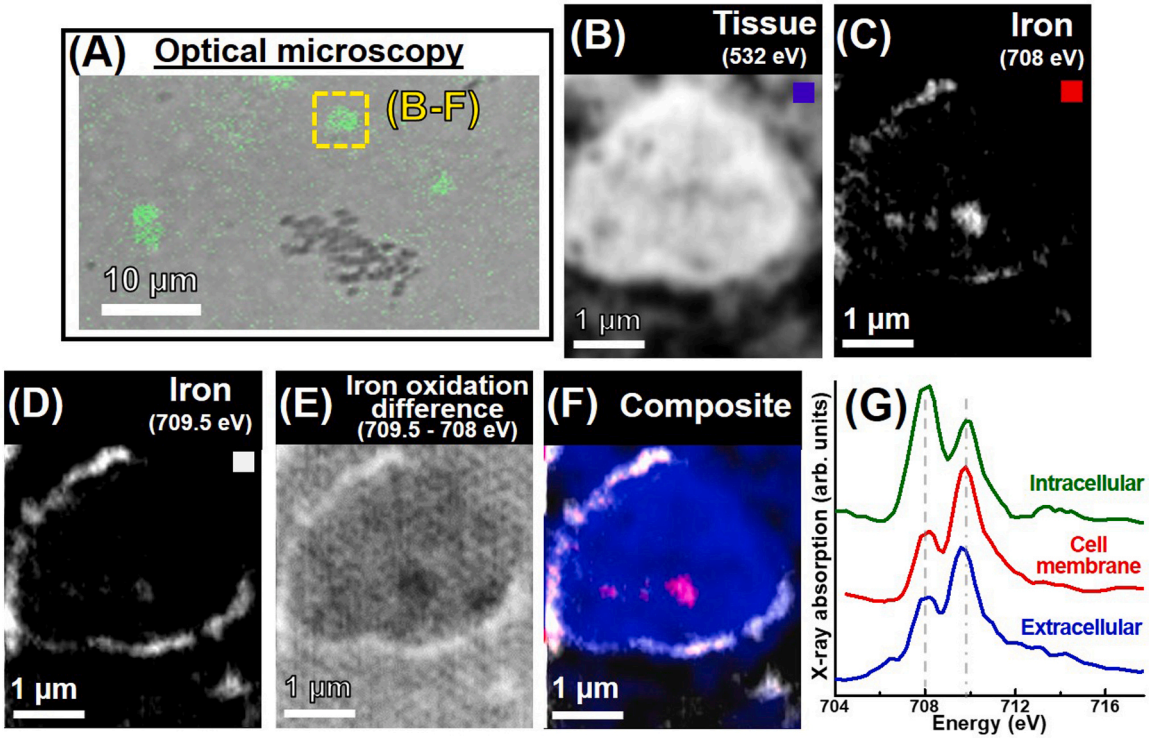

Fig. 6. STXM examination of a cell within a Parkinson's disease tissue section. **(A)** Optical microscopy image, showing areas of high RNA content in green, indicating the presence of cellular material. (B-F) STXM speciation maps and images of the cell highlighted by the yellow box in (A). **(B)** Oxygen *K*-edge tissue map showing cell ultrastructure. **(C)** 708 eV iron L_3-edge speciation map. **(D)** 709.5 eV iron L_3-edge speciation map. **(E)** Iron L_3-edge oxidation state difference map showing strongly absorbing oxidized iron (Fe^{3+}) as light contrast, and chemically reduced iron (Fe^{2+} and/or Fe^0) as dark contrast. **(F)** Composite image showing tissue (blue), 708 eV iron (red) and 709.5 eV iron (grey) content of the glial cell. **(G)** Iron L_3 x-ray absorption spectra from the intracellular (green trace) and cell membrane (red trace) iron content of the cell. The blue spectrum is from extracellular iron content immediately surrounding the cell. The dashed and dotted dashed lines highlight the principal energies corresponding to low oxidation state (708 eV; Fe^{2+} and/or Fe^0) and oxidized (709.5 eV Fe^{3+}) iron respectively.
Data acquired at Diamond Light Source beamline I08.

tissues, careful fitting of STXM experimental data at the Ca *L*-edge allows for calcium phases of differing crystallinity to be selectively imaged (e.g. amorphous cf. crystalline $CaCO_3$) using crystal field splitting as demonstrated in [19]. Further, x-ray linear dichroism can be exploited to study the crystal orientation of carbonates, allowing the selective imaging of differing crystal orientations using STXM via polarization-dependent imaging contrast (PIC) [20].

9.3. Probing iron speciation in tissue

The human central nervous system utilizes iron for many essential processes including neurotransmitter synthesis, nerve impulse propagation, and energy production [21]. Iron chemistry in biological systems can vary dramatically. To fully understand iron biochemistry in these systems, nanoscale resolution imaging and chemical sensitivity are essential.

At the iron $L_{2,3}$-edge, differing iron phases produce markedly different x-ray absorption spectra [22], allowing the discrimination of differing oxidation states and mineral phases in highly localized (<100 nm in this instance) regions of interest. In addition, by using circularly polarized x-rays, the magnetic properties of regions of interest can be characterised via the x-ray magnetic circular dichroism (XMCD) effect [5].

Fig. 6 shows optical microscopy and STXM analysis of adjacent 500 nm thick sections of substantia nigra from a Parkinson's disease case. Fig. 6A is an optical microscopy image from a tissue section stained for RNA content, confirming the presence of cellular material. Fig. 6B-G shows STXM analysis of the cell highlighted by the yellow box in Fig. 6A. By comparing the oxygen *K*-edge tissue ultrastructure (Fig. 6B) to the iron L_3-edge speciation maps (Fig. 6C-D), iron can be seen to be accumulated both intracellularly and within the cell membrane. By examining the iron oxidation difference map (Fig. 6E), where strongly absorbing oxidized iron (Fe^{3+}) is shown as light contrast and chemically reduced iron (Fe^{2+} and/or Fe^0) is shown as dark contrast, variations in iron oxidation state are evident at differing cellular regions. From this map, iron associated with the cell membrane is seen to be predominantly ferric (Fe^{3+}), whereas the intracellular iron is in a low oxidation state (ferrous (Fe^{2+}) or metallic (Fe^0)).

Iron L_3-edge x-ray absorption spectra from these cellular regions are shown in Fig. 6G, and confirm that iron located in the cell membrane (red spectrum) was predominantly ferric, whereas intracellular iron was predominantly ferrous or metallic (green spectrum), with minor ferric

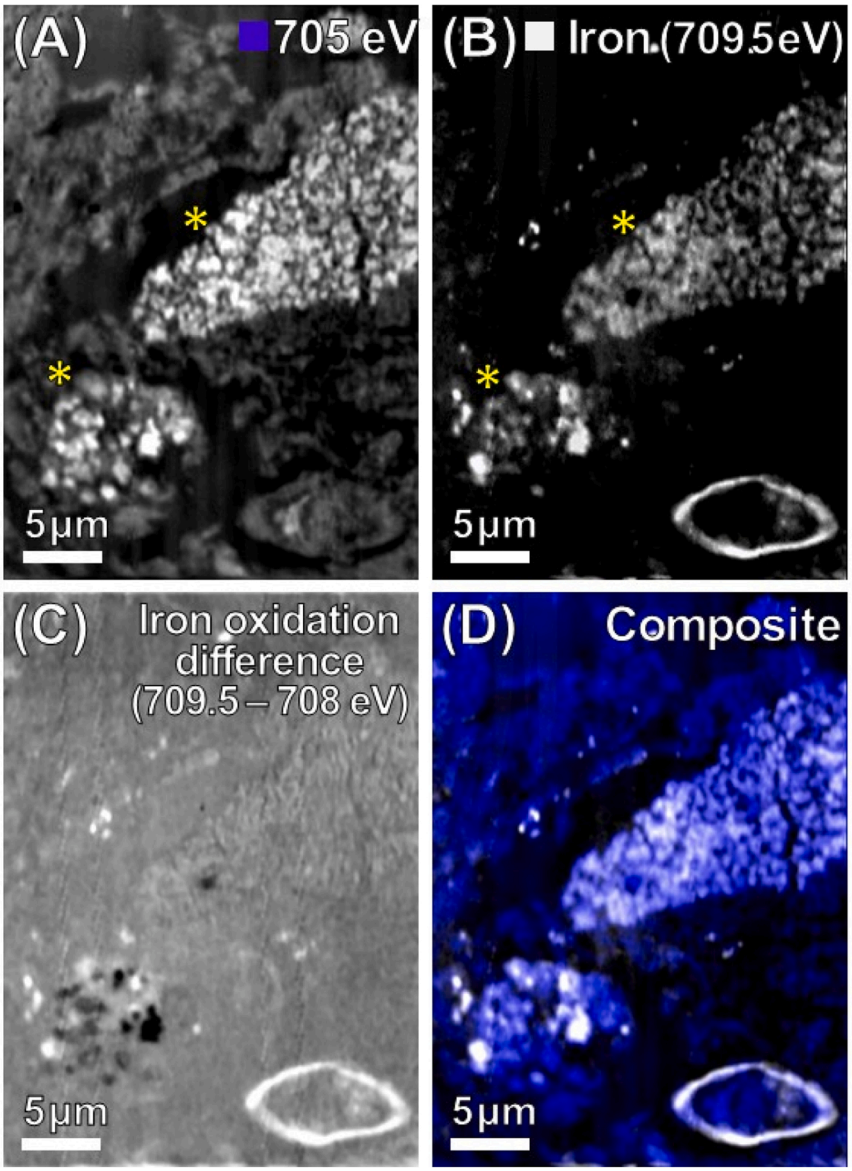

Fig. 7. Iron L_3-edge STXM analysis of a 500 nm thick section of Parkinson's disease substantia nigra. **(A)** Single energy 705 eV image showing overall sample morphology. **(B)** Iron L_3-edge map. In (A) and (B) the asterisks highlight NM-containing dopaminergic neurons. **(C)** Iron L_3-edge oxidation state difference map showing strongly absorbing oxidized iron (Fe^{3+}) as light contrast, and chemically reduced iron (Fe^{2+} and/or Fe^0) as dark contrast. **(D)** Composite image showing sample morphology in blue and iron content in grey.
Data acquired at Diamond Light Source beamline I08.

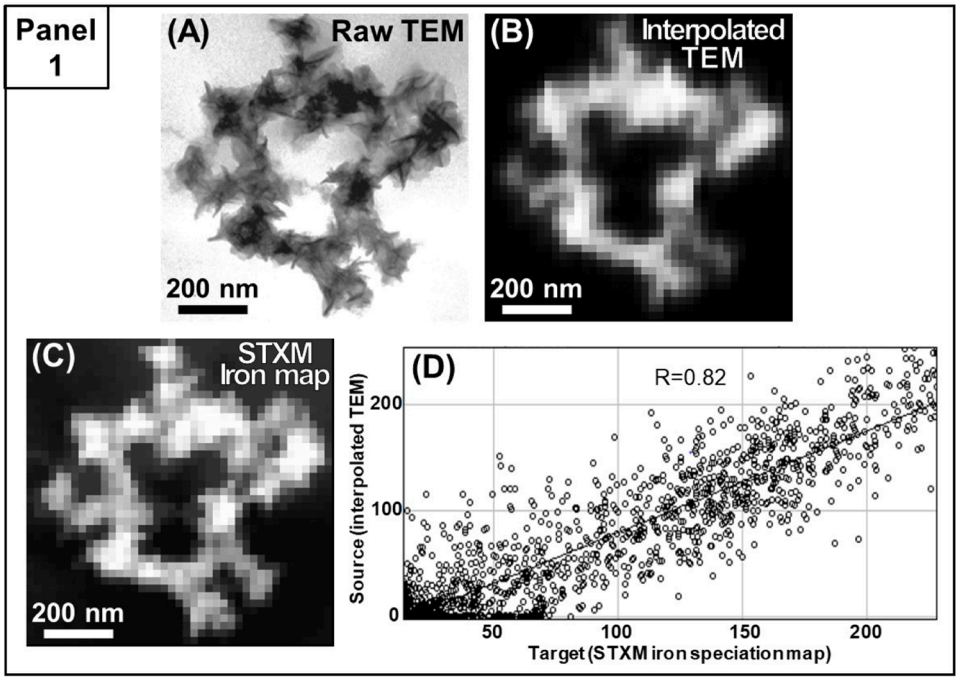

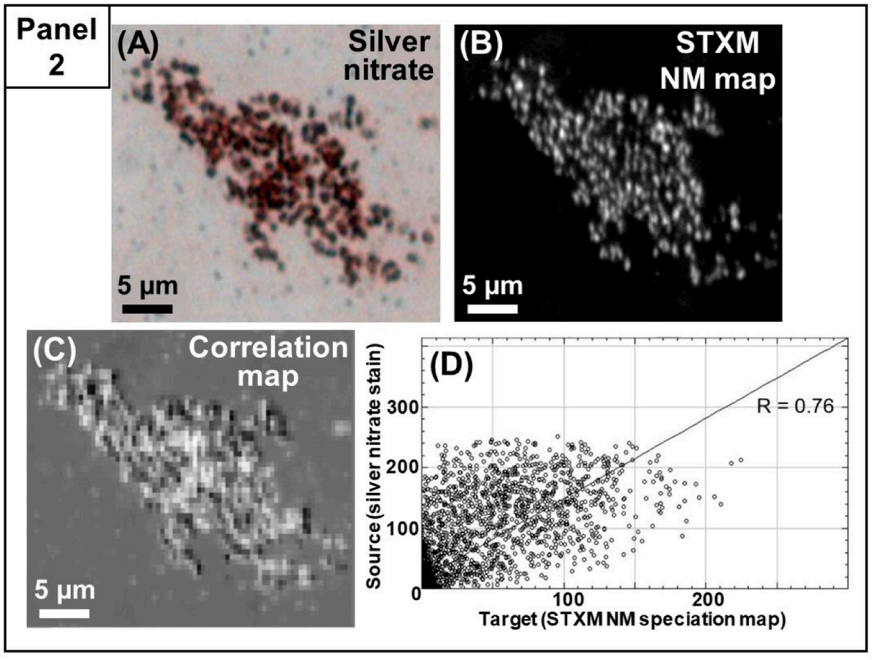

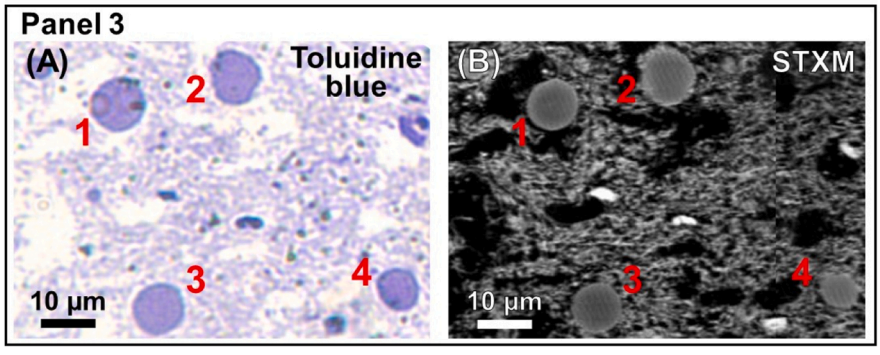

Fig. 8. Examples of correlative microscopy datasets incorporating STXM images. **Panel 1:** TEM and STXM micrographs of an amyloid aggregate structure within a mouse cortical brain tissue section. **(A)** Raw TEM image. **(B)** Bilinear interpolation, resolution adjusted TEM image where resolution is 20 nm. **(C)** 20 nm resolution Iron L_3-edge STXM speciation map. **(D)** Correlation plot for non-zero values, yielding a correlation coefficient of 0.82. **Panel 2:** Light microscopy and STXM micrographs of neuromelanin within adjacent 200 nm thick sections of substantia nigra. **(A)** Optical microscopy silver nitrate stain (165 nm resolution). **(B)** Neuromelanin STXM speciation map (acquired at 200 nm resolution, adjusted using bilinear interpolation to 165 nm resolution). **(C)** Correlation map, where brightest spots show strongest correlation. **(D)** Correlation plot for non-zero values, yielding a correlation coefficient of 0.76. **Panel 3:** Light microscopy and STXM micrographs of tissue ultrastructure within adjacent 500 nm thick sections of amygdala. **(A)** Toluidine blue-stained light microscopy image. **(B)** Oxygen *K*-edge STXM tissue map. Corpora amylacea (examples of which are labelled 1–4), are easily identifiable across both image types.
(a) Data acquired at Canadian Light Source SM beamline. (b) Data acquired at Diamond Light Source beamline I08. (c) Data acquired at Diamond Light Source beamline I08. (d) Modified from Brooks et al. [2,11].

contributions.

Fig. 7 shows further STXM iron L_3-edge analysis of brain tissue from the Parkinson's disease substantia nigra. Here, NM within dopaminergic neurons (highlighted by asterisks in panels (A) and (B)) can be seen to be loaded with iron (Fig. 7B). Iron L_3-edge oxidation difference mapping shows nanoscale variation in NM iron oxidation state (Fig. 7C).

10. Correlative microscopy

The non-destructive nature of STXM allows correlative microscopy to be performed on the same sample section. An example of this can be seen in Fig. 8 Panel 1, where correlative STXM and TEM micrographs from a 200 nm thick brain tissue section are presented. However, care must be taken when considering the order of measurements to prevent changes in native sample chemistry from factors such as high energy of EM beams or the introduction of chemical dyes and contrast agents that could impact the validity of STXM findings. In this example the TEM images were obtained after the STXM analysis was complete.

Another approach for correlative microscopy involves the use of serial tissue sections, where one tissue section remains unstained for STXM analysis and an adjacent section is stained for a desired structure/chemical and examined under e.g. optical microscopy. As section thicknesses required for STXM are typically smaller than the cellular/subcellular features under investigation, the same tissue structures are often identifiable across adjacent sections. Therefore, this approach allows for good correlation between datasets, while also ensuring sample biochemistry is not altered through the addition of dyes and/or contrast agents in sections examined using STXM. This form of correlative microscopy also serves an important function in identifying regions of interest prior to STXM analysis, where experiments are extremely time limited.

Examples of this methodology are shown in Fig. 8 Panels 2 and 3. In Panel 2, image correlation for NM STXM speciation mapping and silver nitrate staining in consecutive sections (200 nm thickness) of substantia nigra is demonstrated. In Panel 3, correlative light microscopy and STXM tissue speciation maps of adjacent tissue sections from the amygdala are displayed. In these images a strong correlation in tissue ultrastructure can be observed across the image types, with the corpora amylacea (examples of which are labelled 1–4) being particularly recognizable in both images.

11. Discussion

11.1. STXM application in neurodegenerative disease research

The versatility and unique capabilities of STXM have allowed us to follow new research directions to understand the remarkable biochemistry of the brain.

Despite playing a vital role in brain function, metals such as iron and copper can convey toxic effects when mishandled, with disrupted brain metal homeostasis being linked to the development of multiple neurodegenerative disorders [23]. Using the methods described above, we recently made the unexpected discovery of elemental metallic copper and ferromagnetic iron nano-deposits within the human brain for the first time [3–5]. These metallic forms have distinctly different chemical and magnetic properties from the oxide forms in which brain metals are predominately stored [21,5,24,25], and their highly reactive surfaces can produce harmful free radicals which are toxic to brain cells [26,27]. The nano-deposits were located within amyloid plaques, a hallmark feature of Alzheimer's disease. Although it is not yet established whether metallic nano-deposits are inherently involved with disease pathogenesis, their discovery raises new questions into the role played by metals in neurochemistry, neurobiology, and in neurodegenerative diseases. In turn, this could facilitate the development of new therapies designed to restore metal balance in diseased brains, potentially slowing or preventing disease progression. In addition, the strong (ferro)magnetic properties of elemental metallic iron could be exploited as endogenous biomarkers for disease diagnosis using techniques such as magnetic resonance imaging (MRI).

The ability to probe combined organic and inorganic deposits will prove important in understanding a host of different diseases. NM containing cells are degenerated in Parkinson's disease, and it has been hypothesized that NM–iron complexes released upon cell death may induce a vicious cycle of chronic inflammation exacerbating neuronal loss contributing to disease progression [2]. Thus, visualising NM in both the healthy and diseased brain tissues and investigating their chemical properties in situ is of particular interest to researchers. As previously mentioned, we showed that label-free nanoscale visualization of neuromelanin and associated metal ions in human brain tissue can be achieved using synchrotron x-ray spectromicroscopy [2]. We used STXM to investigate the chemical state of neuromelanin-bound iron in Parkinson's disease substantia nigra [2]. STXM revealed evidence for mixed oxidation states of neuronal iron deposits associated with neuromelanin clusters including chemically-reduced phases. This chemically-reduced iron could contribute to disease progression through the production of free radicals as described above, and is in contrast to the ferric form in which neuromelanin iron is physiologically stored.

12. Future direction

The development of cryogenically cooled STXM endstations offers the exciting possibility for the measurement of frozen hydrated brain (derived) tissue samples. CryoSTXM removes the need to embed tissue specimens in resin thus better preserving native ultrastructure and biochemistry, allowing measurement of tissues under conditions resembling the living state. Cryofixation methodology must be chosen carefully to obtain the cooling rates required for water vitrification and the formation of amorphous ice. Such high cooling rates prevent deleterious ice crystal formation which negatively impacts on the preservation of native sample ultrastructure [28]. For thinner samples (e.g. cell monolayers) this can be achieved through plunge freezing into a liquid cryogen [29]. For higher volume tissue samples (up to 200 μm thickness), high pressure freezing can be applied. Dependent on sample type, follow up procedures post cyrofixation may be required to produce samples suitable for cryoSTXM such as: (i) cryosectioning using an cryo-ultramicrotome; (ii) freeze fracturing [28]; (iii) the creation of thin lamallea using Cryo-focused-ion-beam (FIB) milling [30], including the newly described Plasma FIB milling approach [31].

Furthermore, cryogenic environments may help protect samples from localized heating effects induced by STXM measurements, allowing greater tolerances to x-ray photon doses, and improved data quality [32] The use of frozen hydrated sample types for STXM analysis creates opportunity for correlative synchrotron analysis in 2D and 3D (using e.g. cryo x-ray tomography). Finally, planned upgrades to synchrotron light sources (such as those proposed for Diamond II) promise greater levels of sensitivity and faster scan times, meaning statistically significant sample measurements between sample types (e.g. disease cf. disease-free brain tissue) may soon be technically feasible.

In summary, we have presented here a novel synchrotron x-ray spectromicroscopy methodology for the nanoscale chemical analysis of human brain tissue, made possible through the combined imaging resolution and chemical sensitivity of STXM, providing new insights into neurobiology and the aetiology of neurodegenerative disease, which may open new avenues for the treatment of these disorders.

Declaration of Competing Interest

The authors declare that they have no known competing financial interests or personal relationships that could have appeared to influence the work reported in this paper.

Data Availability

The datasets from this study are available through the Keele University research repository at http://doi.org/10.21252/vhwf-ta02, and the Warwick Research Archive Portal at https://wrap.warwick.ac.uk/176613/.

Acknowledgements

We thank B. Kaulich, T. Araki, and M. Kazemian for their support at Diamond Light Source beamline I08, T. Tyliszczak and D. Vine for support at the Advanced Light Source beamline 11.0.2, and J. Schwenke, K. Thånell and the support staff at MAX IV SoftiMAX beamline. The Advanced Light Source is supported by the Director, Office of Science, Office of Basic Energy Sciences, of the U.S. Department of Energy under contract no. DE-AC02–05CH11231. We acknowledge MAX IV Laboratory for time on Beamline SoftiMAX under Proposal 20210927. Research conducted at MAX IV, a Swedish national user facility, is supported by the Swedish Research council under contract 2018–07152, the Swedish Governmental Agency for Innovation Systems under contract 2018–04969, and Formas under contract 2019–02496. The Canadian Light Source is funded by the Canada Foundation for Innovation, the Natural Sciences and Engineering Research Council of Canada, the National Research Council Canada, the Canadian Institutes of Health Research, the Government of Saskatchewan, Western Economic Diversification Canada, and the University of Saskatchewan.

Funding

This work was supported by the following: Engineering and Physical Sciences Research Council grants EP/N033191/1 (J.F.C) and EP/N033140/1 (N.D.T). J.B was supported by Engineering and Physical Sciences Research Council Doctoral Training Award EP/N509796/1, Warwick-Wellcome QBP Covid Relief Funding, and Alzheimer's Research UK. J.E was supported by Alzheimer's Research UK (ARUK-ECRBF2022A-017), Keele University Faculty Research Fund, and University of Warwick alumni donations. EH was supported by a Biotechnology and Biological Sciences Research Council-funded doctoral training award and a Race Against Dementia Fellowship funded by the Barbara Naylor Foundation, in collaboration with ARUK.

References

[1] T. Vanderah, D. Gould. Nolte's The Human Brain, eighth ed., Elsevier, 2020.
[2] J. Brooks, J. Everett, F. Lermyte, V. Tjendana Tjhin, S. Banerjee, P.B. O'Connor, C. M. Morris, P.J. Sadler, N.D. Telling, J.F. Collingwood, Label-free nanoimaging of neuromelanin in the brain by soft x-ray spectromicroscopy, Angew. Chem. Int. Ed. 59 (2020) 11984–11991.
[3] J. Everett, V. Tjendana Tjhin, J. Brooks, F. Lermyte, I. Hands-Portman, J. Dobson, J. Collingwood, N. Telling, Nanoscale examination of biological tissues using x-ray spectromicroscopy, Microsc. Microanal. 24 (2018) 490–491.
[4] J. Everett, J.F. Collingwood, V. Tjendana-Tjhin, J. Brooks, F. Lermyte, G. Plascencia-Villa, I. Hands-Portman, J. Dobson, G. Perry, N.D. Telling, Nanoscale synchrotron x-ray speciation of iron and calcium compounds in amyloid plaque cores from Alzheimer's disease subjects, Nanoscale 10 (2018) 11782–11796.
[5] J. Everett, F. Lermyte, J. Brooks, V. Tjendana-Tjhin, G. Plascencia-Villa, I. Hands-Portman, J.M. Donnelly, K. Billimoria, G. Perry, X. Zhu, P.J. Sadler, P.B. O'Connor, J.F. Collingwood, N.D. Telling, Biogenic metallic elements in the human brain? Sci. Adv. 7 (2021) eabf6707.
[6] N.D. Telling, J. Everett, J.F. Collingwood, J. Dobson, G. van der Laan, J. J. Gallagher, J. Wang, A.P. Hitchcock, Iron biochemistry is correlated with amyloid plaque morphology in an established mouse model of Alzheimer's disease, Cell Chem. Biol. 24 (1205–1215) (2017), e3.
[7] J. Cosmidis, K. Benzerara, N. Nassif, T. Tyliszczak, F. Bourdelle, Characterization of Ca-phosphate biological materials by scanning transmission X-ray microscopy (STXM) at the Ca $L_{2,3}$-, P $L_{2,3}$- and C K-edges, Acta Biomater. 12 (2015) 260–269.
[8] J. Stewart-Ornstein, A.P. Hitchcock, D. Hernández Cruz, P. Henklein, J. Overhage, K. Hilpert, J.D. Hale, R.E.W. Hancock, Using intrinsic X-ray absorption spectral differences to identify and map peptides and proteins, J. Phys. Chem. B 111 (2007) 7691–7699.
[9] F. Frati, M.O.J.Y. Hunault, F.M.F. de Groot, Oxygen K-edge X-ray Absorption Spectra, Chem. Rev. 120 (2020) 4056–4110.
[10] L. Zecca, C. Bellei, P. Costi, A. Albertini, E. Monzani, L. Casella, M. Gallorini, L. Bergamaschi, A. Moscatelli, N.J. Turro, M. Eisner, P. Raimondo Crippa, S. Ito, K. Wakamatsu, W.D. Bush, W.C. Ward, J.D. Simon, F.A. Zucca, New melanic pigments in the human brain that accumulate in aging and block environmental toxic metals, PNAS 105 (2008) 17567–17572.
[11] J. Brooks, J. Everett, F. Lermyte, V. Tjendana Tjhin, P.J. Sadler, N.D. Telling, J. F. Collingwood, Analysis of neuronal iron deposits in Parkinson's disease brain tissue by synchrotron x-ray spectromicroscopy, J. Trace Elem. Med. Biol. 62 (2020), 126555.
[12] M. Riba, E. Augé, J. Campo-Sabariz, D. Moral-Anter, L. Molina-Porcel, T. Ximelis, R. Ferrer, R. Martín-Venegas, C. Pelegrí, J. Vilaplana, *Corpora amylacea* act as containers that remove waste products from the brain, *PNAS* 116 (2019) 26038–26048.
[13] J.B. Cavangh, Corpora-amylacea and the family of polyglucosan diseases, Brain Res. Rev. 29 (1999) 265–295.
[14] K. Kahil, S. Weiner, L. Addadi, A. Gal, Ion pathways in biomineralization: perspectives on uptake, transport, and deposition of calcium, carbonate, and phosphate, J. Am. Chem. Soc. 143 (2021) 21100–21112.
[15] T.J.B. Simons, Calcium and neuronal function, Neurosurg. Rev. 11 (1988) 119–129.
[16] Y.U.T. Gong, C.E. Killian, I.C. Olson, N.P. Appathurai, A.L. Amasino, M.C. Martin, L.J. Holt, F.H. Wilt, P.U.P.A. Gilbert, Phase transitions in biogenic amorphous calcium carbonate, *PNAS* 109 (2012) 6088–6093.
[17] S.J. Natel, T.,K. Sham, Y.M. Yiu, B.W. Yates, Calcium L-edge XANES study of some calcium compounds, J. Synchrotron Radiat. 8 (2001) 255–257.
[18] F.M. LaFerla, Calcium dyshomeostasis and intracellular signalling in Alzheimer's disease, Nat. Rev. Neurosci. 3 (2002) 862–872.
[19] M. Katsikini, E. Proiou, N. Vouroutzis, F. Pinakidou, E.C. Paloura, D. Smirnov, M. Brzhezinskaya, S. Ves, Crystalline and amorphous calcium carbonate as structural components of the *Calappa granulate* exoskeleton, J. Struct. Biol. 211 (2020), 107557.
[20] Y.H. Lo, J. Zhou, A. Rana, D. Morrill, C. Gentry, B. Enders, Y. Yu, C. Sun, D. A. Shapiro, R.W. Falcone, H.C. Kapteyn, M.M. Murnane, P.U.P.A. Gilbert, J. Miao, X-ray linear dichroic ptychography, PNAS 118 (2021), e2019068118.
[21] J.R. Connor, S.L. Menzies, J.R. Burdo, P.J. Boyer, Iron and iron management proteins in neurobiology, Pediatr. Neurol. 25 (2001) 118–129.
[22] T.J. Regan, H. Ohldag, C. Stamm, F. Nolting, J. Lüning, J. Stöhr, R.L. White, Chemical effects at metal/oxide interfaces studied by x-ray-absorption spectroscopy, Phys. Rev. B 64 (2001), 214422.
[23] R.J. Ward, F.A. Zucca, J.H. Duyn, R.R. Crichton, L. Zecca, The role of iron in brain ageing and neurodegenerative disorders, Lancet Neurol. 13 (2014) 1045–1060.
[24] P. Jiang, D. Prendergast, F. Borondics, S. Porsgaard, L. Giovanetti, E. Pach, J. Newberg, H. Bluhm, F. Besenbacher, M. Salmeron, Experimental and theoretical investigation of the electronic structure of Cu_2O and CuO thin films on Cu(110) using x-ray photoelectron and absorption spectroscopy, J. Chem. Phys. 138 (2013), 024704.
[25] N.D. Telling, G. van der Laan, M.T. Georgieva, N.R.S. Farley, Facility for combined in situ magnetron sputtering and soft x-ray magnetic circular dichroism, Rev. Sci. Instrum. 77 (2006), 073903.
[26] D.B. Kell, Iron behaving badly: Inappropriate iron chelation as a major contributor to the aetiology of vascular and other progressive inflammatory and degenerative diseases, BMC Med. Genom. 2 (2009) 2.
[27] J. Prousek, Fenton chemistry in biology and medicine, Pure Appl. Chem. 79 (2007) 2325–2338.
[28] D. Struder, B.M. Humbel, M. Chiquet, Electron microscopy of high pressure frozen samples: bridging the gap between cellular ultrastructure and atomic resolution, Histochem. Cell Biol. 130 (2008) 877–889.
[29] C.A. Okolo, I. Kounatidis, J. Groen, K.L. Nahas, S. Balint, T.M. Fish, M.A. Koronfel, A.L. Cortajarena, I.M. Dobbie, E. Pereiro, M. Harkiolaki, Sample preparation strategies for efficient correlation of 3D SIM and soft X-ray tomography data at cryogenic temperatures, Nat. Protoc. 16 (2021) 2851–2885.
[30] F.R. Wagner, R. Wantanabe, R. Schampers, D. Singh, H. Persoon, M. Schaffer, P. Fruhstorfer, J. Plitzko, E. Villa, Preparing samples from whole cells using focussed-ion-beam milling for cryo-electron tomography, Nat. Protoc. 15 (2020) 2041–2070.
[31] C. Berger, M. Dumoux, T. Glen, N.B. Yee, J.M. Mitchels, Z. Patáková, M.C. Darrow, J.H. Naismith, M. Grange, Plasma FIB milling for the determination of structures in situ, Nat. Commun. 14 (2023) 629.
[32] A. Hitchcock, H. Yuan, L. Melo, N. Basim, Soft X-ray scanning transmission microscopy studies of radiation damage by electron, ion and X-ray beams, Microsc. Microanal. 26 (2020) 2072–2074.